## **Unsupervised Learning on Monocular Videos for 3D Human Pose Estimation**

Sina Honari<sup>1\*</sup>, Victor Constantin<sup>1</sup>, Helge Rhodin<sup>2</sup>, Mathieu Salzmann<sup>1</sup>, Pascal Fua<sup>1</sup>

<sup>1</sup>CVLab, EPFL, Lausanne, Switzerland

<sup>2</sup>Imager Lab, UBC, Vancouver, Canada

## **Abstract**

In the presence of annotated data, deep human pose estimation networks yield impressive performance. Nevertheless, annotating new data is extremely time-consuming, particularly in real-world conditions. Here, we address this by leveraging contrastive self-supervised (CSS) learning to extract rich latent vectors from single-view videos. Instead of simply treating the latent features of nearby frames as positive pairs and those of temporally-distant ones as negative pairs as in other CSS approaches, we explicitly disentangle each latent vector into a time-variant component and a time-invariant one. We then show that applying CSS only to the time-variant features, while also reconstructing the input and encouraging a gradual transition between nearby and away features, yields a rich latent space, well-suited for human pose estimation. Our approach outperforms other unsupervised single-view methods and matches the performance of multi-view techniques.

## 1. Introduction

While supervised body pose estimation is rapidly becoming a mature field, the bottleneck remains the availability of sufficiently large training datasets, which cannot be guaranteed for many kinds of human motions. An effective way to address this is to leverage unsupervised data to learn a low-dimensional representation of poses. Then, it only takes very little annotated data to train a regressor to predict 3D poses from this representation. Key to the success is a good unsupervised learning objective, for which many existing techniques exploit the availability of multiview footage [21, 30, 36, 24, 22]. However, recording with multiple synchronized cameras increases complexity.

In this paper, we introduce an alternative unsupervised representation learning strategy for human pose estimation using videos acquired by a *single* RGB camera. To this end, we build on the idea of contrastive self-supervised (CSS) learning [20, 9, 3]. For any given sample, CSS aims to

maximize the similarity to a positive sample and the dissimilarity to a negative one. In our context, one way to do so is to treat a video frame close to the one of interest as positive, and a temporally-distant one as negative [1, 25]. Unfortunately, this simple strategy is insufficient because it does not account for the fact that, when someone moves, some features, such as garment appearance, remain constant over time, even as the person's pose changes. As a result, contrastive learning should be applied only to the features changing across time and not to all features.

To overcome this, we learn a representation that explicitly separates each latent vector into a *time-variant* component and a *time-invariant* one. We then exploit CSS learning to capture the fact that the time-variant component evolves smoothly. Hence, the time-variant components of two poses that are close in time should, in general, be more similar than those of poses that are temporally distant, independently of the fact that the time-invariant components should remain stable. Fig. 1 summarizes our approach.

It differs from typical CSS strategies in four ways: First, we encourage a gradual transition from temporally close to temporally distant frames. Second, we apply our contrastive formulation only to the time-variant components. Third, we perform image re-synthesis by mapping the latent vectors back to images to improve the quality of the learned latent features. Finally, when observing subjects in free fall such as divers, we incorporate a gravity-encoding prior to help with detection of the subject. Our experiments demonstrate that these four components help the model learn in an unsupervised manner a rich, low-dimensional latent representation of human motions from ordinary video sequences acquired using standard monocular RGB cameras.

Given this representation, a mapping to 3D pose can be learned from a very limited amount of annotated data. We demonstrate the benefits of our approach for pose estimation on four real-world RGB datasets. It outperforms other unsupervised monocular approaches and yields results on par with unsupervised multi-view setups, while being much easier to deploy. In particular, it can exploit both monocular and multi-view videos when available, which a purely multi-view setup cannot, and can handle changing back-

<sup>\*</sup>sina.honari@epfl.ch

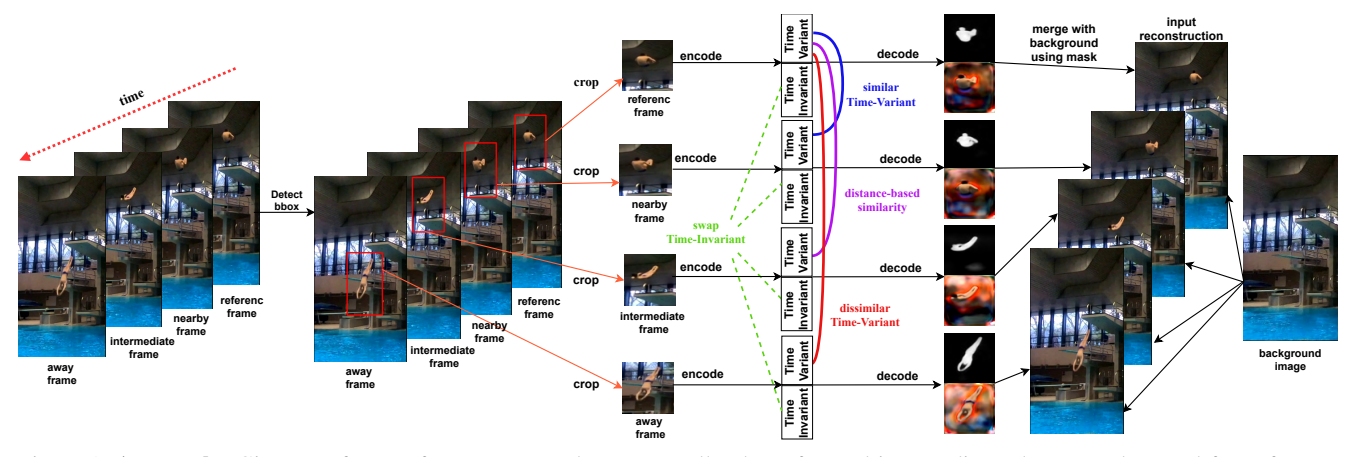


Figure 1. **Approach.** Given a reference frame, we sample a temporally close, far, and intermediate—between close and far —frames. The model first detects the person in all frames using a spatial transformer network. The detected regions are then cropped and encoded into *time-variant* and *time-invariant* components. The time-variant of the reference frame is made similar to that of the nearby frame and dissimilar to that of the away frame, while a distance-dependent similarity or dissimilarity is enforced between the reference and intermediate frames. To promote invariance of the time-invariant components, they are swapped with other frames in the video. The model then decodes each frame into a segmentation mask and an image. The decoded image is then merged with the background using the bounding box location and the decoded mask. No annotations are used (neither for detection, nor for segmentation) and the same network weights are used for all frames. At test time, the model can process a single frame.

grounds. The disentangled latent representation also lends itself for editing operations, such as pose and appearance transfer. We will make our code publicly available.

## 2. Related Work

Unsupervised and self-supervised learning [2, 5] techniques have received considerable attention in recent years as a means to decrease the amount of annotated data required to train deep networks. We briefly review some of the methods most closely related to our work.

**Single-View Approaches.** Unsupervised learning for general video processing has been extensively researched. For example, LSTMs have been used to learn representations of video sequences [26]. Similarly, optical-flow and color diversity across frames has been leveraged to learn latent features corresponding to motion and appearance [31]. Multiple papers [17, 14, 6, 34] use the temporal order of frames to learn latent features from videos. In particular, the models of [17, 6] classify whether a set of frames have correct ordering or not, whereas those of [14, 34] predict the order of the frames or clips as a classification task. In [32], instead of relying on temporal ordering, a model is trained to predict the pace of a video subsampled at different rates. This work also leverages a CSS loss across clips, where positive pairs are clips from the same video and negative pairs are clips from different ones. None of these techniques, however, were designed for pose estimation. For example, predicting temporal order [17, 14, 6, 34] is best suited for activity recognition, for which the order of the observed event truly matters. Similarly, the contrastive learning strategy used in [32] aims to extract features that are invariant across video frames, whereas, to predict a continuously changing body pose, we need to capture variations between the frames.

Several works have nonetheless focused on extracting time-varying features, yet in different contexts. Harley *et al.* [7] use RGB and depth from n time-steps to map 2.5D features to a 3D latent space, and then use the camera pose at time-step n+1 to predict the 2D latent features for that time-step. While [7] exploits depth, other works [25, 1, 3] leverage CSS, with [25, 1] using it in single-view videos. However, they do no use any decoder to reconstruct the images from the latent features, thus opening the door to losing valuable information about the observed context. We will demonstrate that for the pose estimation task our encoding/decoding approach yields richer features.

Unsupervised learning methods have also been developed for 2D keypoint estimation [28, 35, 33, 12, 27, 15, 13]. Some of these [35, 33, 12, 15, 13] learn separate features for pose and appearance, as we do. However, being designed for 2D keypoint estimation, they either explicitly detect 2D keypoints or generate heatmaps, and extending them to 3D pose estimation remains unadressed. Furthermore, whereas we learn to detect our subject without supervision, these methods rely on ground-truth bounding box locations.

The approach most closely related to ours is DrNet [4], which disentangles each frame into pose and content. DrNet uses a discriminator that distinguishes frames extracted from the same video from ones extracted from different videos and encourages the encoder to produce latent repre-

sentations that do not carry any information about whether they come from the same or different videos. This, however, fails in cases where the two videos feature different kinds of activities—for example, running in one and sitting on the floor in the other. In this scenario, the pose still indicates if the frames come from the same video or not, which precludes disentanglement.

Multi-View Approaches. The difficulty of performing unsupervised learning using a single camera has led to the development of several multi-view approaches [36, 19, 25, 29, 23, 22]. While some multi-view approaches are semisupervised [24, 18], here, we focus only on fully unsupervised learning, where no pose labels are used when training the self-supervised model. Among unsupervised methods, the strategy of [23, 22] is closest in spirit to ours. It uses a multi-camera setup to learn a latent-representation that disentangles appearance and pose, where pose should remain similar when rotated across different views and appearance should remain the same across different videos of the same person. This unsupervised training scheme makes it possible to encode an image into a low-dimensional latent vector. As shown in [23, 22], an effective mapping from this latent space to 3D poses can be learned from only a small amount of annotated data. Our approach operates on the same general principle, but we learn the latent representation from videos acquired by a single camera, which makes it easier to deploy.

## 3. Method

Our goal is to extract rich latent features, without any supervision, from single-camera videos featuring people. We aim to capture information only about the foreground subjects and to leverage the similarity or dissimilarity of frames given their distance in time. A key observation is that global object appearance tends to remain constant over time while pose usually changes from frame to frame, which is something our latent vectors should reflect.

To this end, given a video database without annotations, we train an encoder that splits latent features into *time-variant* and *time-invariant* components. The latter captures features that remain consistent over time, such as person's clothing and appearance, while the former models the time-changing elements in each frame, such as body pose. This enables us to define a similarity measure that accounts for the different behavior of these two components and to implement an effective contrastive-learning procedure that produces latent vectors useful for human pose estimation. Without this split, the latent components learned using similarity measures would be unable to reliably differentiate vectors for temporally away frames, since no matter how distant they are, they still share information.

By contrast, popular approaches to using CSS [20, 1,

25, 3] neither learn time-invariant components nor try to reconstruct the input images. Hence, no decoding occurs on the learned latent features. We will demonstrate that this approach yields worse results. In other words, splitting latent vectors while leveraging contrastive learning is a unique feature of our approach. Another is an attention mechanism that separates foreground from background and integrates gravity as a supervisory signal when possible. In the remainder of this section, we discuss the different components of our approach in detail.

## 3.1. Model Architecture and Training

We aim to address real-world applications where the foreground subject is small and occupies only a fraction of the image. To this end, we use a neural network architecture with an attention mechanism to separate foreground from background. As shown in Fig. 2, given an input image I. a spatial transformer network (STN) [11]  $\mathcal{S}$  extracts four parameters that define the subject's bounding box, two non-homogeneous scales  $s^x, s^y$  and its center coordinates  $u^x, u^y$ , yielding  $S(\mathbf{I}) = (s^x, s^y, u^x, u^y)$ . These parameters are used to crop an image patch  $I_{crop}$  that is passed to a timeinvariant encoder  $\mathcal{E}_{ti}$  such that  $\mathcal{E}_{ti}(\mathbf{I}_{crop}) = \mathbf{I}_{ti}$ , where  $\mathbf{I}_{ti}$  is the time-invariant component of the latent vector for image  ${f I}.$  A color-jittered version of the crop  ${f I}_{crop}$  is passed to the time-variant encoder  $\mathcal{E}_{tv}$  such that  $\mathcal{E}_{tv}(\hat{\mathbf{I}}_{crop}) = \mathbf{I}_{tv}$  with  $\mathbf{I}_{tv}$ the time-variant latent component. Both encoders share parameters except at the output layer. A decoder  $\mathcal{D}$  then takes  $\mathbf{I}_{tv}$  and  $\mathbf{I}_{ti}$  as inputs and decodes them into a mask  $\mathbf{M}_{crop}$ and an RGB crop  $\mathbf{D}_{\text{crop}}.$  The mask and RGB crops are then used to re-synthesize a full-resolution image by using the inverse transformation of the STN and merging the result with a background image B. This operation can be written

$$\tilde{\mathbf{I}} = \mathbf{M} \times \mathbf{D} + (1 - \mathbf{M}) \times \mathbf{B} , \qquad (1)$$

where  $\tilde{\mathbf{I}}$  is the reconstructed image. Fig. 2 depicts this process. Note that no labels are used here, neither for detection, nor for segmentation. We train the networks  $\mathcal{S}$ ,  $\mathcal{E}$ , and  $\mathcal{D}$  such that they jointly accomplish three goals:

- Encoding information that relates only to the fore-ground object (Section 3.1.1);
- Disentangling the time-variant and time-invariant components (Section 3.1.3);
- Encoding time-variant components such that they are more similar for poses that are close in time than for temporally distant ones (Section 3.1.2).

## 3.1.1 Reconstruction Loss

To compare the reconstructed image from Eq. (1) with the original one, we use the L2 loss on the image pixels as well

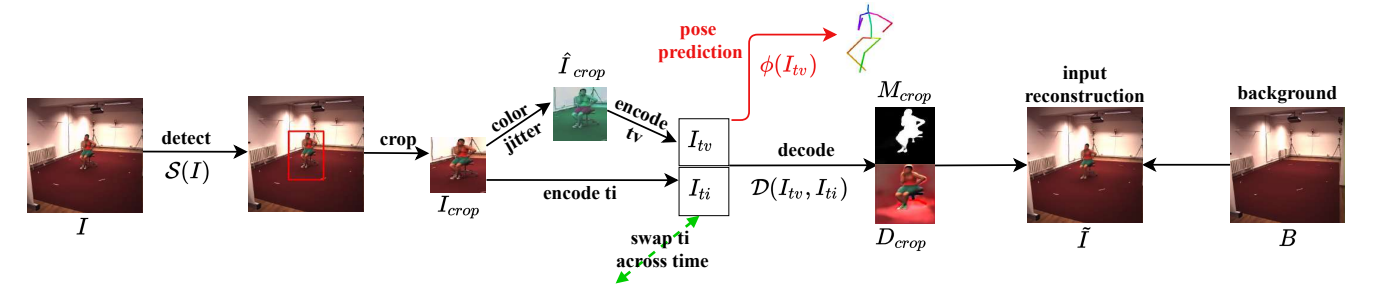


Figure 2. **Model architecture.** Using spatial transformer network (STN) S, a bounding box is detected and cropped on an input image I. The cropped image,  $I_{crop}$ , is then passed to an encoder  $\mathcal{E}_{ti}$  that predicts time-invariant  $I_{ti}$  component. This component is swapped across time with other frames to enforce disentanglement. A color jittered variant of the crop  $\hat{I}_{crop}$  is passed to another encoder  $\mathcal{E}_{tv}$  to predict time-variant  $I_{tv}$  features. Both encoders share parameters, except in the output layer. The combined features are then passed to a decoder  $\mathcal{D}$  that outputs a mask  $M_{crop}$  and RGB crop  $D_{crop}$ . These two outputs are then put to the image resolution using inverse STN operation and then merged with background  $\mathbf{B}$  to output the reconstruct image  $\tilde{\mathbf{I}}$ . This constitutes the self-supervised model, which is then frozen. In the second phase (shown in red), predicted  $I_{tv}$  is passed to a shallow network  $\Phi$  to predict the pose.

as on the features extracted of layers 1 to 3 of the ResNet18 [8] model as

$$\mathcal{L}_{\text{reconst}} = \lambda \|\mathbf{I} - \tilde{\mathbf{I}}\|_{2}^{2} + \rho \sum_{l=1}^{3} \|\text{Res}_{l}(\mathbf{I}) - \text{Res}_{l}(\tilde{\mathbf{I}})\|_{2}^{2}. \quad (2)$$

As discussed above, we use a background image when resynthizing the input image, hence this reconstruction loss encourages our latent representation to focus on the foreground object.

## 3.1.2 Contrastive Loss

To encourage time-variant components that are close in time to be close to each other and those that are far in time not to be, we rely on a contrastive loss. Many current CSS approaches [3, 20, 1] first take a reference input  $\mathbf{I}$ , a positive sample  $\mathbf{I}^+$ , and n-1 negative samples  $\mathbf{I}^-_k$  for  $1 \le k < n$ , and then minimize the loss

$$\mathcal{L}_{CSS} = -\log \frac{\exp(\text{sim}(\mathcal{F}(\mathbf{I}), \mathcal{F}(\mathbf{I}^{+}))/\tau)}{\sum_{k=1}^{n} \exp(\text{sim}(\mathcal{F}(\mathbf{I}), \mathcal{F}(\mathbf{I}_{k}^{-/+}))/\tau)}, \quad (3)$$

where  $\mathbf{I}_k^{-/+}$  indicates a set of one positive and n-1 negative examples.  $\mathcal{F}(\mathbf{I})$  represents the features encoded by the network  $\mathcal{F}$  given frame  $\mathbf{I}$  as input and  $\text{sim}(\mathbf{m}, \mathbf{n}) = (\mathbf{m}^T \mathbf{n})/(\|\mathbf{m}\| \|\mathbf{n}\|)$ . In [25], the contrastive loss is defined instead as a triplet loss

$$\mathcal{L}_{\text{CSS}} = \left[ \| \mathcal{F}(\mathbf{I}) - \mathcal{F}(\mathbf{I}^+) \|^2 + \beta \right] < \| \mathcal{F}(\mathbf{I}) - \mathcal{F}(\mathbf{I}^-) \|^2 , \quad (4)$$

with  $\beta>0$ , meaning that the squared L2 distance between a positive pair should be smaller than that between a negative one by at least  $\beta$ . However, neither definitions of  $\mathcal{L}_{CSS}$  above define the loss relative to the temporal distance of the frames. This is what we change by introducing a distance-based similarity loss.

**Distance-based Similarity Loss (DSL).** Our goal is to compare every pair of samples directly and to define a loss that enforces similarity or dissimilarity between any two samples depending on their temporal proximity.

Let  $\mathbf{I}_{tv}^m$  and  $\mathbf{I}_{tv}^n$  be the time-variant component of the vectors extracted from two images captured at times  $t_m$  and  $t_n$ . If  $|t_m-t_n|$  is small, we would like  $\mathrm{sim}(\mathbf{m},\mathbf{n})$ , where  $\mathrm{sim}()$  is the similarity function used in Eq. (3), to be close to one. By contrast, if  $|t_m-t_n|$  is larger than a threshold distance  $d_{\max}$ , we would like  $\mathrm{sim}(\mathbf{m},\mathbf{n})$  to be zero. To this end, we introduce the loss function

$$\mathcal{L}_{DSL}(\mathbf{I}_{tv}^{m}, \mathbf{I}_{tv}^{n}) =$$

$$\begin{cases} (1 - \frac{2d}{d_{max}}) |1 - \sin(\mathbf{I}_{tv}^{m}, \mathbf{I}_{tv}^{n})|, & \text{if } 0 \leq d \leq d_{max}/2, \\ \min(\frac{2d}{d_{max}} - 1, 1) |\sin(\mathbf{I}_{tv}^{m}, \mathbf{I}_{tv}^{n})|, & \text{otherwise,} \end{cases}$$

where  $d = |t_m - t_n|$  is the temporal distance between the two frames. As shown in Fig. 3,  $\mathcal{L}_{DSL}$  is piecewise linear in terms of  $sim(\mathbf{I}_{tv}^m, \mathbf{I}_{tv}^n)$ . It favors similarity for  $0 \le d \le d_{max}/2$ , and dissimilarity for  $d > d_{max}/2$ .

In practice, to learn time-variant components in our framework, for any given reference input frame  $\mathbf{I}^r$ , we sample three other frames, a nearby one  $\mathbf{I}^n$  (positive sample), a far away one  $\mathbf{I}^a$  (negative sample taken at least at  $d_{\max}$ ), and an intermediate one,  $\mathbf{I}^{in}$  (acquired after  $\mathbf{I}^n$  and before  $\mathbf{I}^a$ ). We then compute

$$\mathcal{L}_{DSL}^{all} = \mathcal{L}_{DSL}(\mathbf{I}_{tv}^r, \mathbf{I}_{tv}^n) + \mathcal{L}_{DSL}(\mathbf{I}_{tv}^r, \mathbf{I}_{tv}^a) + \mathcal{L}_{DSL}(\mathbf{I}_{tv}^r, \mathbf{I}_{tv}^{in}) + \mathcal{L}_{DSL}(\mathbf{I}_{tv}^r, \mathbf{I}_{tv}^{in}) .$$
 (6)

The above loss allows us to compare the reference frame with similar, dissimilar, and intermediate frames directly.

## 3.1.3 Disentanglement

Note that our DSL only acts on the time-variant components, and thus does not encourage a split between time-variant and time-invariant information. To force the network to disentangle these two types of components, we

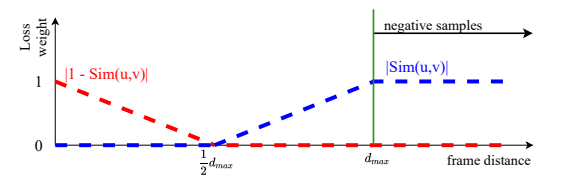


Figure 3. **Distance-based Similarity Loss (DSL).** The red line shows the **weight**,  $(1-\frac{2d}{d_{\max}})$ , applied to  $|\mathrm{sim}(\mathbf{m},\mathbf{n})-1|$  when two frames are close (similarity measure) and the blue line shows the **weight**,  $\min(\frac{2d}{d_{\max}}-1,1)$ , applied to  $|\mathrm{sim}(\mathbf{m},\mathbf{n})|$  when the frames are away (dissimilarity measure). Both weights depend on the temporal distance between the frames. As the frame distance increases, the similarity weight is reduced, eventually going to zero at  $d_{\max}/2$ , and the dissimilarity weight increases, eventually reaching one at  $d_{\max}$ , the frame from which negative samples are taken.

swap the time-invariant ones across time with different frames during training. This prevents the time-invariant components from encoding information about the subject's pose. We also use a color-jittered variant of the cropped image  $\hat{\mathbf{I}}_{\text{crop}}$  that is used to predicts the time-variant features  $\mathbf{I}_{tv}$ . It helps the  $\mathcal{E}_{tv}$  encoder to focus on the pose and not the texture when predicting  $\mathbf{I}_{tv}$ .

## 3.2. Gravity as a Supervisory Signal

The work reported here was initially motivated by a project that involves modeling competitive divers in free fall. In this context, since the falling person is subject to gravity, we can leverage Newtonian mechanics as follows.

While in free fall, a person's center of gravity (CG) is subject to gravitational acceleration. Ignoring the air resistance that remains small until the diver reaches the water,  $\mathbf{p}(t)$ , the CG location at time t, can be written as  $\mathbf{p}(t) = 0.5\mathbf{g}t^2 + \mathbf{v}_0t + \mathbf{p}_0$ , where  $\mathbf{g}$  is a usual gravitational vector,  $\mathbf{v}_0$  the CG initial speed, and  $\mathbf{p}_0$  its initial location. We know neither  $\mathbf{v}_0$  and  $\mathbf{p}_0$  nor when the jump started. Nevertheless, we can leverage the fact that the acceleration, that is, the second derivative of  $\mathbf{p}$  is constant and equal to  $\mathbf{g}$ . To this end, we only need to consider four *equidistant* times  $t_1, t_2, t_3, t_4$ . We can approximate the acceleration at  $t_2$  and  $t_3$  using finite differences and write that they should be equal. This yields  $\mathcal{L}_{\text{track}}$ . Please check the supplementary material for detail.

## 3.3. Training and Inference

To train our network, we adjust the weights of the networks  $\mathcal{S}$ ,  $\mathcal{E}$ , and  $\mathcal{D}$  introduced in Section 3.1 to minimize the total training loss

$$\mathcal{L}_{\text{total}} = \mathcal{L}_{\text{reconst}} + \alpha \mathcal{L}_{\text{DSL}}^{\text{all}} + \gamma \mathcal{L}_{\text{track}} , \qquad (7)$$

where  $\mathcal{L}_{reconst}$  of Eq. (2) favors a good image reconstruction,  $\mathcal{L}_{DSL}^{all}$  of Eq. (6) applies a contrastive loss, and  $\mathcal{L}_{track}$ 



Figure 4. Swapping time-invariant and time-variant components. In each column, the time-invariant component is taken from the image on the top, and the time-variant component is taken from the image on the bottom and concatenated to generate the image shown in bottom, using the decoder.

of Eq. (14) is used when the subject is in free fall. During the minimization, we permute randomly the time-invariant components of the latent vectors to promote disentanglement as described in Section 3.1.3. This part of the training is unsupervised.

Once the unsupervised model is trained, its parameters are frozen and we use a small number of images with corresponding ground-truth poses for supervised training of a simple two-layer perceptron  $\Phi$  designed to associate a pose vector to the time-variant latent vector  $\mathbf{I}_{tv}$  that the encoder  $\mathcal{E}$  has extracted from image  $\mathbf{I}$ . To this end, we adjust the weights of  $\Phi$  by minimizing

$$\mathcal{L}_{\text{pose}} = \frac{1}{N} \sum_{k=1}^{N} \|\Phi(\mathbf{I}_{tv}^k) - \mathbf{q}^k\|^2 , \qquad (8)$$

where  $\mathbf{I}_{tv}^k$  is the time-variant vector associated to the  $k^{th}$  image and  $\mathbf{q}^k$  the corresponding ground-truth pose, in cameracoordiante and pelvis centered, represented by a concatenation of the Cartesian coordinates of body joints.

## 4. Experimental Results

In this section, we present the baseline models and compare our approach to these models on human pose estimation. Please check the supplementary material for model architecture and experimental details.

#### 4.1. Disentanglement

In Figure 4, we show samples obtained by merging time-variant and time-invariant components from different sources to reconstruct new images. The disentanglement is obtained by swapping time-invariant features across time and jittering the color of the time-variant components, as discussed in Section 3.1.3.

## 4.2. Quantitative Results

Unless otherwise stated, for all models we use the latent representation learned in a self-supervised manner and train an MLP with 2 hidden layers taking a latent vector as input, as discussed in Section 3.3. At this stage, the self-supervised models are frozen and only the pose models are trained. For the models that split the latent features, we use the time-variant component for pose estimation. For the models that don't, we use all latent features. We report the results using the normalized mean per joint position error (N-MPJPE), expressed in mm.

## Baseline Models We compare our model to:

- CSS [1, 3]: Single-view CSS loss using Eq. (3) without image reconstruction or splitting the latent space into  $I_{tv}$  and  $I_{ti}$  components.
- MV-CSS [25]: Mutli-view CSS loss using the triplet loss of Eq. (4), also without reconstruction or splitting.
- **DrNet** [4]: Single-view approach using both reconstruction and latent splitting. It uses a discriminator for latent splitting.
- NSD [22]: Multi-view approach that performs both reconstruction and latent splitting.

and against variants of our own approach:

- AE-STN: This variant of our model uses STN together with an auto-encoding image-reconstruction, but without contrastive training or latent splitting.
- **CSS-STN:** This variant of our model uses STN together with image-reconstruction and latent splitting. However, it uses Eq. (3) instead of Eq. (5) for the contrastive loss.
- **CSS-DSL:** This is our approach using STN together with image-reconstruction and latent splitting. It uses Eq. (5) for the contrastive loss.

All of these models are trained with the same backbone architecture and model capacity, so that only the training loss differentiates them. For MV-CSS, we follow the recommendation in [25] to sample one positive sample from another view at the same timestamp, and one negative sample from a distant frame in the same video. For CSS and CSS-STN, we use one positive sample from a nearby-frame and two negative samples from away frames from the same video. For DSL-STN, we replace one of the away frames with an intermediate frame, sampled between nearby and away frames. We follow the procedures in [4, 22] to train DrNet and NSD.

	Model	Decodes?	Percentage of Labeled Pose Data					
	Model	Decoues:	0.3% (100)	1% (500)	14% (5K)	50% (17K)	all (35K)	
	MV-CSS [25]	Х	216.15	206.08	203.24	202.65	202.52	
MV	NSD [22]	✓	140.92	115.37	94.48	91.01	88.89	
	CSS [1, 3]	Х	230.77	215.96	197.22	195.70	194.69	
SV	DrNet [4]	✓	158.81	126.18	108.21	106.41	100.38	
	AE-STN	/	187. 25	161.53	130.21	117.044	114.73	
	CSS-STN	/	163.61	137.52	110.61	104.23	99.32	
	DSL-STN (Ours)	/	149.32	122.44	100.23	97.38	95.39	

Table 1. Comparison against baselines on the PoseTrack H36M test-set. The top rows characterize the unsupervised multi-view (MV) models and the bottom rows the single-view (SV) ones. The last 5 columns show N-MPJPE results when using different percentage of labeled 3D pose samples. The value in parenthesis are the corresponding number of images with labels.

#### 4.2.1 Human3.6M [10] (H36M)

Following the protocol of [22], we use subjects 1, 5, 6, 7, and 8 to train the self-supervised models. We subsample every 5 frames of the training set, as done in [22], which yields 308,760 frames.

Comparative 3D pose estimation results. We follow the same procedure as in [22] for 3D human pose estimation within the PoseTrack2018 challenge setup. It comprises 35,832 training images with pose labels and 19,312 test samples. We compare our results to those of other unsupervised models in Table 1 and report the N-MPJPE as a function of the percentage of labeled pose samples being used. We consistently outperform the other single-view methods and come close to NSD, even though it uses multiple views. Note that the models without decoding, whether single- or multi-view perform poorly on this task.

**Ablation Study.** We perform an ablation study by removing different model components in the same experimental setup as in Table 1. We report our results in Table 2.

In the first two rows, we remove the reconstruction loss and only train the model with the DSL loss term. The performance drops considerably, indicating the importance of image reconstruction in learning rich features. Since the model does not reconstruct the image, it cannot learn the time-invariant components, so all the latent components are time-variant. The number of latent features in these models is equivalent to that in the model that uses time-variant and time-invariant features, so there is no capacity change.

In the third row, we have a model that reconstructs the input but does not apply a latent split. The performance is also reduced, showing that splitting the latent space is beneficial in learning better time-variant features, as the model can apply the contrastive loss only to the time-variant component. Finally, in the fourth row, we change only the DSL loss of Eq. (5) to the CSS loss of Eq. (3) and still observe a performance drop. In summary, all the proposed modules have a role and disabling any of them reduces performance.

**2D keypoint estimation.** As discussed in Section 2, some 2D keypoint estimation approaches [35, 27, 15, 13] separate

Decodes?	uses STN?	contrastive loss	latent split?	Percentage of Labeled Pose Data				
Decodes:				0.3% (100)	1% (500)	14% (5K)	50% (17K)	all (35K)
X	X	DSL	X	227.24	220.64	198.34	193.08	191.21
X	/	DSL	X	236.32	211.85	202.57	199.16	198.22
✓	/	DSL	×	185.75	159.34	135.93	129.62	127.52
✓	/	CSS	/	163.61	137.52	110.61	104.23	99.32
<b>✓</b>	/	DSL	/	149.32	122.44	100.23	97.38	95.39

Table 2. **Ablation Study.** The last row shows our full model with all features applied. In the first two rows we remove the decoding part. In this setting since the model is not reconstructing the image from the latent features it can only learn the time-variant features, hence the latent-split cannot be applied. In the third row, we keep all the features except we do not split the latent components. In the fourth row, we only change the contrastive loss from DSL to CSS. In all settings, we observe a performance drop, however, the models without decoding suffer the most.

Model	2D keypoint error
Thewlis et al. [27]	7.51
Zhang et al. [35]	4.14
Lorenz et al. [15]	2.79
Jakab et al. [13]	2.73
DSI-STN (Ours)	2.53

Table 3. Comparison against stateof-the-art 2D models on H36M dataset. %-MSE normalized by image size is reported. All models predict 32 keypoints on 6 actions of wait, pose, greet, direct, discuss, and walk.

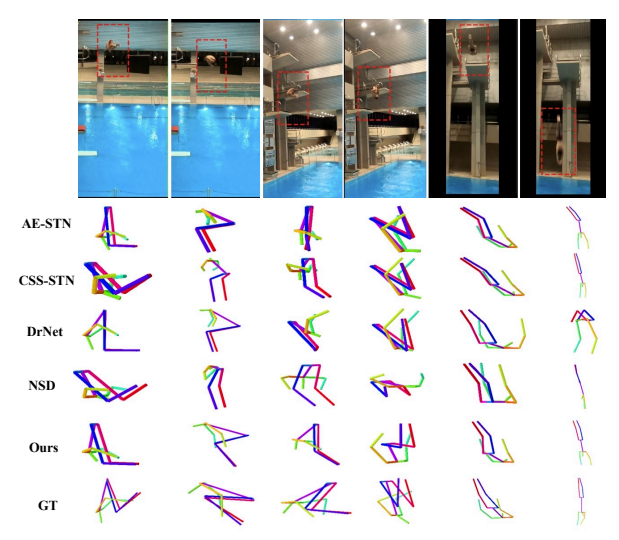


Figure 5. Qualitative results on the Diving Dataset. Samples are taken from the test set at different stages of dive. The red region shows the bounding box detected by our model for image cropping. GT in the bottom row indicates the ground truth labels.

features for pose and appearance, as we do. For comparison purposes, we therefore also evaluate our extracted timevariant features for 2D keypoint estimation, using the same setup as in Table 1 of [13], that is, we train a single linear layer from the time-variant features to the 2D keypoints. As in [13], we use subjects 1,5,6,7,8 for training and 9,11 for testing. As can be seen in Table 3, our model outperforms the others.

## 4.2.2 MPI-INF-3DHP [16] (MPI)

On this dataset, we consider two settings:

MV-data: The self-supervised model is trained on subjects S1 to S8, which are multi-view. Since the test-videos have different backgrounds compared to the training ones, we train the self-supervised models on random background images to help the model generalize to new backgrounds. To this end, we take random images from the Internet as background and put the subject in-front of them, using the foreground mask of

the dataset. Note that these masks are just used to create input images are not used in the models.

All-data: Since the self-supervised models do not require labels, we can leverage all data to train them, whether single or multi-view. This corresponds to a transductive learning setting. In this case, the self-supervised model is trained using \$1 to \$8 (multi-view) and \$T\$1 to \$T\$4 (single-view).

The datasets are subsampled every 5 frames, yielding 198,096 training frames in the MV-data case and 202,905 training frames in all-data case.

In both settings, to train the pose estimation MLP, we use subjects S1, S2, S3, S4, S5, S8 as training set, and S6 and S7 as validation set. For testing, we use TS1 to TS4. Because there are many pose labels, we use at most 2% of the pose data for training, that is, 17,128 images. The test set comprises 2207 frames. We report the results in Table 4. As the S1 to S8 videos are multi-view and the TS1 to TS4 ones are single-view, we can only evaluate NSD in the MV-data setting. Our model again performs closely to NSD in this setting with the advantage that, because our approach is single-view, we can also train on the TS1 to TS4 videos, thus further improving performance. In a practical setting, this means that we could exploit additional videos as they become available, whether or not they are multiview, something NSD cannot do.

	Model	Percentage of Labeled Pose Data					
	Model	.02% (171)	.1% (856)	.2% (1712)	5% (4K)	2%(17K)	
	AE-STN	279.00	258.73	256.27	251.92	246.57	
MV-data	CSS-STN	274.45	255.91	252.45	246.64	242.92	
	NSD [22]	256.34	241.12	239.81	237.56	235.61	
	DSL-STN (Ours)	261.99	245.09	241.34	239.48	236.85	
	AE-STN	245.87	230.98	225.42	220.19	206.98	
All-data	CSS-STN	243.83	223.85	218.62	208.25	203.69	
	DrNet [4]	253.47	243.87	233.09	228.09	218.18	
	DSL-STN (Ours)	235.62	219.72	211.26	202.60	192.11	

Table 4. Comparing against baselines on MPI-INF-3DHP. N-MPJPE results on pose prediction as a function of the quantity of annotated data. The top rows show results in the MV-data setting, where the self-supervised models have access only to multi-view data. The bottom rows show results in the All-data setting where self-supervised models have access to both multi-view and single-view data. Note that, in this scenario, our results are now better than those of NSD because it can also exploit single-view data.

#### 4.2.3 Diving Dataset

We acquired video sequences featuring a male and a female competitive divers. The dataset contains dives with heights of 3, 5, 7.5, and 10 meters, and is captured with both multicamera and single-camera setups. We use both subjects to train the self-supervised model, yielding 19,464 training frames, of which 16,469 frames are multi-view. NSD is trained on multi-view videos while all other models are trained on all frames.

To train the pose model, for all methods we use the female subject for training, by splitting the videos into training and validation sets, and the male for testing. As a result, we can use up to 2,419 frames for supervised training, 2,288 frame for validation, and 2,112 frames for testing. We report the accuracy of the models in Table 5. On this dataset, our approach outperforms all the other methods including the multi-view NSD. While NSD can only leverage multiview videos, our approach can benefit from both multi- and single-view, hence leveraging more available data. It also outperforms the variant AE-STN and CSS-STN, which is in line with the results presented in Section 4.2.1. We also present a variant of our model without the tracking loss (DSL-STN (no  $\mathcal{L}_{track}$ )), which shows a performance drop if this component is not used. Note that  $\mathcal{L}_{track}$  is only used on this dataset, where there is a free fall. We show some pose prediction results in Fig. 5. Please check the supplementary material for further visualization.

Model		Percentage of Labeled Pose Data					
Model		5% (120)	10% (241)	20% (483)	50% (1209)	100% (2419)	
Multi-View	NSD [22]	270.42	238.23	221.25	200.28	195.13	
Muiti-view	DSL-STN (Ours)	279.82	242.78	224.45	205.89	197.40	
	AE-STN	320.93	295.65	277.96	266.64	257.19	
	CSS-STN	289.52	264.45	247.35	227.28	211.17	
All-data	DrNet [4]	320.07	290.93	271.87	258.14	248.31	
	DSL-STN (no $\mathcal{L}_{track}$ )	296.22	268.88	255.02	236.49	225.77	
	DSL-STN (Ours)	265.09	232.66	216.14	197.82	186.45	

Table 5. Comparison against baselines on the Diving dataset. N-MPJPE results as a function of the quantity of annotated data used to train the pose predictor. Top two rows show models trained only on multi-view data. The bottom rows show models trained using both single-view and multi-view data.

#### 4.2.4 Ski Dataset

To check the performance of our model given a changing background, we evaluate our model on a ski dataset [24] where the camera follows skiers down the slope. It features 6 skiers, each going down a slalom course twice. We use Subjects 1 to 5 for training and Subject 6 to evaluate the models. This yields 3,124 images for training and 636 images for testing. To generate background images, we compute the homography matrix relating consecutive frames and stitch them into the panorama shown in the supplementary material, from which we extract the desired background image. In Fig. 6 we show three sample frames, the

corresponding estimated backgrounds, and the backgroundsubtracted images. Note that, because of noise, background subtraction does not yield images containing only the subject of interest. The model still needs to learn to focus on the subject and ignore the remaining background. We further show samples of detected masks, reconstructed images, and 3D pose estimates. In Table 6, we show that our approach outperforms the best performing single-view models. Check the supplementary material for more results.

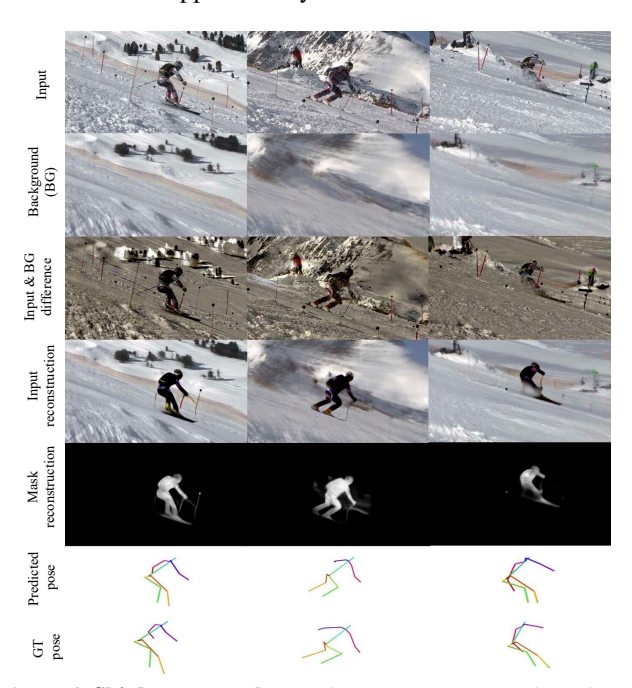


Figure 6. **Ski dataset results.** In the top two rows we show three input images sampled from the test-set and the corresponding estimated background images. In the third row we show the background subtracted input images, in which some of the background details are still present. In the next three rows, we show the output of our model, that is, the reconstructed images, the predicted masks, and the estimated poses.

Model	DrNet [4]	CSS-STN	DSI-STN (Ours)
N-MPJPE	180.31	134.29	113.20

Table 6. Comparison on ski dataset.

## 5. Conclusion

In this work, we have presented an unsupervised feature extraction model for monocular videos. It applies contrastive learning to the time-variant components of the input, which, together with an additional image decoding, allows it to extract richer features than standard CSS approaches. Our framework is designed to extract features from the foreground object, and is thus well-suited to human pose estimation. We have evidenced this on four benchmark datasets where our approach was shown to outperform other single-view self-supervised learning strategies and to match the performance of multi-view ones.

**Acknowledgment.** This work was supported in part by Innosuisse, the Swiss Innovation Agency. We also would like to thank SwissTiming for their support and cooperation in this project.

## References

- [1] Ankesh Anand, Evan Racah, Sherjil Ozair, Yoshua Bengio, Marc-Alexandre Côté, and R Devon Hjelm. Unsupervised state representation learning in atari. In *Advances in Neural Information Processing Systems*, pages 8769–8782, 2019. 1, 2, 3, 4, 6
- [2] Y. Bengio, A. Courville, and P. Vincent. Representation Learning: A Review and New Perspectives. *IEEE Transactions on Pattern Analysis and Machine Intelligence*, 2013.
- [3] Ting Chen, Simon Kornblith, Mohammad Norouzi, and Geoffrey Hinton. A simple framework for contrastive learning of visual representations. *International Conference on Machine Learning*, 2020. 1, 2, 3, 4, 6
- [4] Emily L Denton et al. Unsupervised learning of disentangled representations from video. In *Advances in Neural Informa*tion Processing Systems, pages 4414–4423, 2017. 2, 6, 7, 8
- [5] C. Doersch and A. Zisserman. Multi-Task Self-Supervised Visual Learning. In *International Conference on Computer Vision*, October 2017. 2
- [6] Basura Fernando, Hakan Bilen, Efstratios Gavves, and Stephen Gould. Self-supervised video representation learning with odd-one-out networks. In *Conference on Computer Vision and Pattern Recognition*, pages 3636–3645, 2017. 2
- [7] Adam W. Harley, Shrinidhi K. Lakshmikanth, Fangyu Li, Xian Zhou, Hsiao-Yu Fish Tung, and Katerina Fragkiadaki. Learning from unlabelled videos using contrastive predictive neural 3d mapping. In *International Conference on Learning Representations*, 2020. 2
- [8] K. He, X. Zhang, S. Ren, and J. Sun. Deep Residual Learning for Image Recognition. In *Conference on Computer Vision and Pattern Recognition*, pages 770–778, 2016. 4, 17
- [9] Aapo Hyvarinen and Hiroshi Morioka. Unsupervised feature extraction by time-contrastive learning and nonlinear ica. In *Advances in Neural Information Processing Systems*, pages 3765–3773, 2016. 1
- [10] C. Ionescu, J. Carreira, and C. Sminchisescu. Iterated Second-Order Label Sensitive Pooling for 3D Human Pose Estimation. In Conference on Computer Vision and Pattern Recognition, 2014. 6
- [11] M. Jaderberg, K. Simonyan, A. Zisserman, and K. Kavukcuoglu. Spatial Transformer Networks. In Advances in Neural Information Processing Systems, pages 2017–2025, 2015. 3
- [12] Tomas Jakab, Ankush Gupta, Hakan Bilen, and Andrea Vedaldi. Unsupervised learning of object landmarks through conditional image generation. In NIPS, 2018. 2
- [13] Tomas Jakab, Ankush Gupta, Hakan Bilen, and Andrea Vedaldi. Self-supervised learning of interpretable keypoints from unlabelled videos. In *CVPR*, pages 8787–8797, 2020. 2, 6, 7

- [14] Hsin-Ying Lee, Jia-Bin Huang, Maneesh Singh, and Ming-Hsuan Yang. Unsupervised representation learning by sorting sequences. In *Conference on Computer Vision and Pat*tern Recognition, pages 667–676, 2017. 2
- [15] Dominik Lorenz, Leonard Bereska, Timo Milbich, and Bjorn Ommer. Unsupervised part-based disentangling of object shape and appearance. In *CVPR*, pages 10955–10964, 2019. 2, 6, 7
- [16] D. Mehta, H. Rhodin, D. Casas, P. Fua, O. Sotnychenko, W. Xu, and C. Theobalt. Monocular 3D Human Pose Estimation in the Wild Using Improved CNN Supervision. In *International Conference on 3D Vision*, 2017. 7
- [17] Ishan Misra, C Lawrence Zitnick, and Martial Hebert. Shuffle and learn: Unsupervised learning using temporal order verification. In *European Conference on Computer Vision*, pages 527–544, 2016. 2
- [18] Rahul Mitra, Nitesh B Gundavarapu, Abhishek Sharma, and Arjun Jain. Multiview-consistent semi-supervised learning for 3d human pose estimation. In CVPR, pages 6907–6916, 2020. 3
- [19] Joel Ruben Antony Moniz, Christopher Beckham, Simon Rajotte, Sina Honari, and Chris Pal. Unsupervised depth estimation, 3d face rotation and replacement. In Advances in Neural Information Processing Systems, pages 9736–9746, 2018. 3
- [20] Aaron van den Oord, Yazhe Li, and Oriol Vinyals. Representation learning with contrastive predictive coding. In arXiv Preprint, 2018. 1, 3, 4
- [21] G. Pavlakos, X. Zhou, K. Derpanis. G. Konstantinos, and D. Kostas. Harvesting Multiple Views for Marker-Less 3D Human Pose Annotations. In *Conference on Computer Vision and Pattern Recognition*, 2017. 1
- [22] H. Rhodin, V. Constantin, I. Katircioglu, M. Salzmann, and P. Fua. Neural Scene Decomposition for Human Motion Capture. In *Conference on Computer Vision and Pattern Recognition*, 2019. 1, 3, 6, 7, 8, 17, 18
- [23] H. Rhodin, M. Salzmann, and P. Fua. Unsupervised Geometry-Aware Representation for 3D Human Pose Estimation. In *European Conference on Computer Vision*, 2018.
- [24] H. Rhodin, J. Spoerri, I. Katircioglu, V. Constantin, F. Meyer, E. Moeller, M. Salzmann, and P. Fua. Learning Monocular 3D Human Pose Estimation from Multi-View Images. In Conference on Computer Vision and Pattern Recognition, 2018. 1, 3, 8
- [25] Pierre Sermanet, Corey Lynch, Yevgen Chebotar, Jasmine Hsu, Eric Jang, Stefan Schaal, Sergey Levine, and Google Brain. Time-contrastive networks: Self-supervised learning from video. In *International Conference on Robotics and Automation*, pages 1134–1141, 2018. 1, 2, 3, 4, 6
- [26] N. Srivastava, E. Mansimov, and R. Salakhudinov. Unsupervised Learning of Video Representations Using LSTMs. In *International Conference on Machine Learning*, pages 843–852, 2015.
- [27] James Thewlis, Samuel Albanie, Hakan Bilen, and Andrea Vedaldi. Unsupervised learning of landmarks by descriptor vector exchange. In *ICCV*, pages 6361–6371, 2019. 2, 6, 7

- [28] James Thewlis, Hakan Bilen, and Andrea Vedaldi. Unsupervised learning of object landmarks by factorized spatial embeddings. In *ICCV*, pages 5916–5925, 2017. 2
- [29] Yonglong Tian, Dilip Krishnan, and Phillip Isola. Contrastive multiview coding. European Conference on Computer Vision, 2020. 3
- [30] H.-Y. Tung, H.-W. Tung, E. Yumer, and K. Fragkiadaki. Self-Supervised Learning of Motion Capture. In Advances in Neural Information Processing Systems, pages 5242–5252, 2017.
- [31] Jiangliu Wang, Jianbo Jiao, Linchao Bao, Shengfeng He, Yunhui Liu, and Wei Liu. Self-supervised spatio-temporal representation learning for videos by predicting motion and appearance statistics. In *Conference on Computer Vision and Pattern Recognition*, pages 4006–4015, 2019. 2
- [32] J. Wang, J. Jiao, and Y. Liu. Self-Supervised Video Representation Learning by Pace Prediction. In European Conference on Computer Vision, 2020. 2
- [33] O. Wiles, A.S. Koepke, and A. Zisserman. Self-supervised learning of a facial attribute embedding from video. In *Brit. Mach. Vis. Conf.*, 2018. 2
- [34] Dejing Xu, Jun Xiao, Zhou Zhao, Jian Shao, Di Xie, and Yueting Zhuang. Self-supervised spatiotemporal learning via video clip order prediction. In *Conference on Computer Vision and Pattern Recognition*, pages 10334–10343, 2019. 2
- [35] Y. Zhang, Y. Guo, Y. Jin, Y. Luo, Z. He, and H. Lee. Unsupervised Discovery of Object Landmarks as Structural Representations. In *Conference on Computer Vision and Pattern Recognition*, pages 2694–2703, 2018. 2, 6, 7
- [36] T. Zhou, M. Brown, N. Snavely, and D. Lowe. Unsupervised Learning of Depth and Ego-Motion from Video. In *Conference on Computer Vision and Pattern Recognition*, pages 1851–1858, 2017. 1, 3

# Unsupervised Learning on Monocular Videos for 3D Human Pose Estimation Supplementary Information

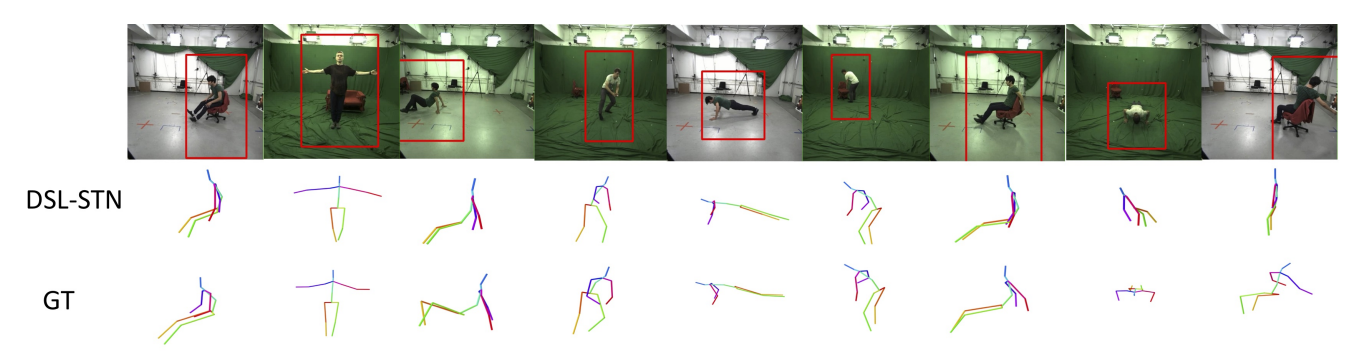


Figure S1. **Qualitative results on MPI Dataset**. Samples are taken from the test set. In the top row, the red rectangle shows the bounding box detected by our model for image cropping. The two bottom rows, respectively show the pose estimation by our model and the ground truth pose. The last two columns show examples with high error.

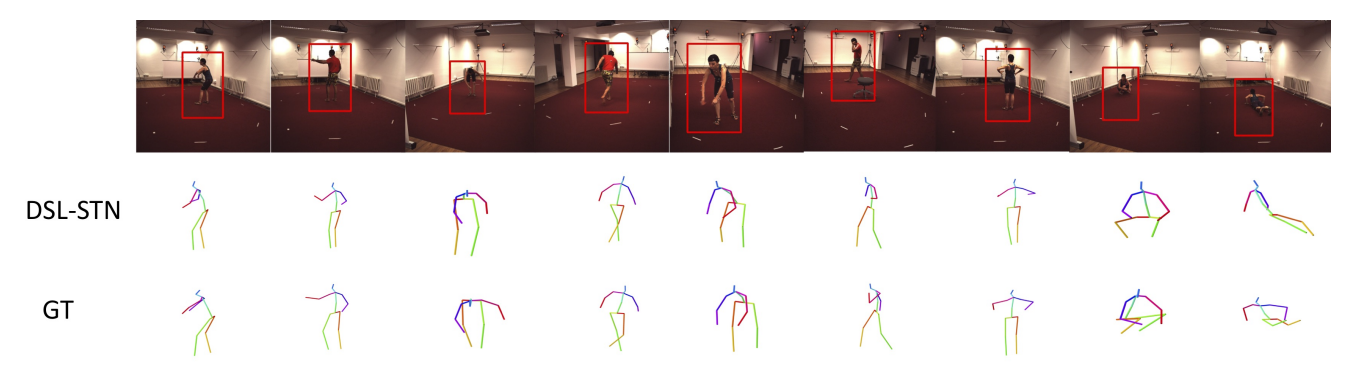


Figure S2. **Qualitative results on H36M Dataset**. Samples are taken from the test set. In the top row, the red rectangle shows the bounding box detected by our model for image cropping. The two bottom rows, respectively show the pose estimation by our model and the ground truth pose. The last two columns show examples with high error.

In this document, we present additional examples on disentangling of pose and appearance, as well as qualitative results on pose estimation. We also present details on the integration of gravity constraints as well as model architecture and training.

## S.1. Qualitative Results

**Disentanglement.** In Figures S3 we take time-invariant component from an image and time-variant component from a different image to reconstruct an output image. As can be observed, the model learns to separate these two components.

**Prediction Samples.** In Figures S2 and S1 we show pose estimation results on H36M and MPI test set. In Figures S4, S5, and S6 we show samples on the Diving dataset.

Figure S7 shows samples of ski dataset. As observed in these examples, background subtraction or thresholding

it does not remove the background and indeed our model learns to focus on the skier. We also show the estimated pose by our model.

## S.2. Tracking Loss Details

Here we elaborate the gravity-aware tracking loss presented in Section 3.2 that encourages constant gravitational acceleration when gravity is the only force acting on subjects in free fall. In practice, two difficulties arise in imposing this constraint. First, equations of motions apply to the center of gravity (CG) of an object but it is not obvious where someone's CG is, as it depends on their posture and on the weight of each body part. Second, we only have access to 2D projections of  $\mathbf{p}(t)$  in the image plane.

Recall from Section 3.1 that our model first applies an STN S, which, for each frame, outputs a bounding box around the subject parameterized by two scales and two



Figure S3. **Swapping time-invariant and time-variant components**. Top two rows show two source images S1 and S2. In each column, in the third row the time-invariant component is taken from S2, and the time-variant component is taken from S1 and concatenated to generate the image shown, using the decoder. In the last row, the sources are swapped. As can be observed the model manages to correctly swap time-invariant and time-variant components. However, due to low-dimensional feature representation of the latent components, not all details are maintained. For examples, the clothes details are lost.

center coordinates,  $s^x$ ,  $s^y$ ,  $u^x$ ,  $u^y$ . We address the first problem by approximating the projection of  $\mathbf{p}(t)$  as the center of the bounding box  $(u^x, u^y)$ . To address the second problem, we consider that the diver's CG travels in a plane. If it were parallel to the image plane or the projection was orthographic, the value of  $u^y$  would vary linearly with the 3D position and so would acceleration. Under these conditions, the following image acceleration relationship would hold exactly. For four equidistant frames  $t_1$ ,  $t_2$ ,  $t_3$ ,  $t_4$ , the acceleration at times  $t_2$  and  $t_3$  in terms of the finite differences approximation is equal to,

$$2\mathbf{p}(t_2) - \mathbf{p}(t_1) - \mathbf{p}(t_3) = 2\mathbf{p}(t_3) - \mathbf{p}(t_2) - \mathbf{p}(t_4)$$
  

$$\Rightarrow 3\mathbf{p}(t_2) - 3\mathbf{p}(t_3) + \mathbf{p}(t_4) - \mathbf{p}(t_1) = 0.$$
 (9)

It implies that

$$3u_2^y - 3u_3^y + u_4^y - u_1^y = 0, (10)$$

where  $u_t^y$  denotes the value of  $u^y$  at time t. Even when the diver does not travel in a plane parallel to the image one or the projection is not orthographic, the frame-to-frame change in distance to the camera of the CG typically remains small and perspective effects are negligible with respect to the vertical motion. Eq.(10) is therefore a good approximation, occuring mostly in y direction as displacement in x is small, which we will show in Section S.3. We therefore impose the constraint of Eq.(10) as a soft constraint only in y direction by adding a new loss term as

$$\mathcal{L}_{\text{const-acc}} = \|(u_1^y + 3u_3^y) - (u_4^y + 3u_2^y)\|^2, \qquad (11)$$

where  $u_t^y$  is the translation predicted in the y direction at time t. This definition does not differentiate between moving up or down, whereas, in practice, we know that the diver goes down. This corresponds to  $u_t^y$  increasing over time. Hence, we also introduce an  $order loss \mathcal{L}_{order}$  that we define as

$$\mathcal{L}_{\text{order}} = \sum_{t=1}^{3} \max \left( 0, \tau - \left( u_{t+1}^{y} - u_{t}^{y} \right) \right) , \qquad (12)$$

where  $\tau$  is a threshold to satisfy a minimum distance between frames t and t+1. In our experiments we set value of  $\tau$  to 20 pixels.

In free-fall, the detector could still make the bounding box bigger to compensate for the aforementioned losses. We therefore prevent the scales  $s_x$  and  $s_y$  of the bounding boxes from varying abruptly from frame to frame by defining a scale loss  $\mathcal{L}_{\text{sc}}$  as

$$\mathcal{L}_{sc} = \sum_{t=1}^{3} \left\| (s_t^x, s_t^y) - (s_{t+1}^x, s_{t+1}^y) \right\|^2.$$
 (13)

Putting this all together, the tracking loss is then equal to

$$\mathcal{L}_{\text{track}} = \mathcal{L}_{\text{const-acc}} + \mathcal{L}_{\text{order}} + \mathcal{L}_{\text{sc}} . \tag{14}$$

## S.3. Acceleration Sensitivity Analysis

An object's location  $\mathbf{p}(t)$  at time t falling down in 3D space using gravity is formulated by  $\mathbf{p}(t) = 0.5\mathbf{g}t^2 +$ 

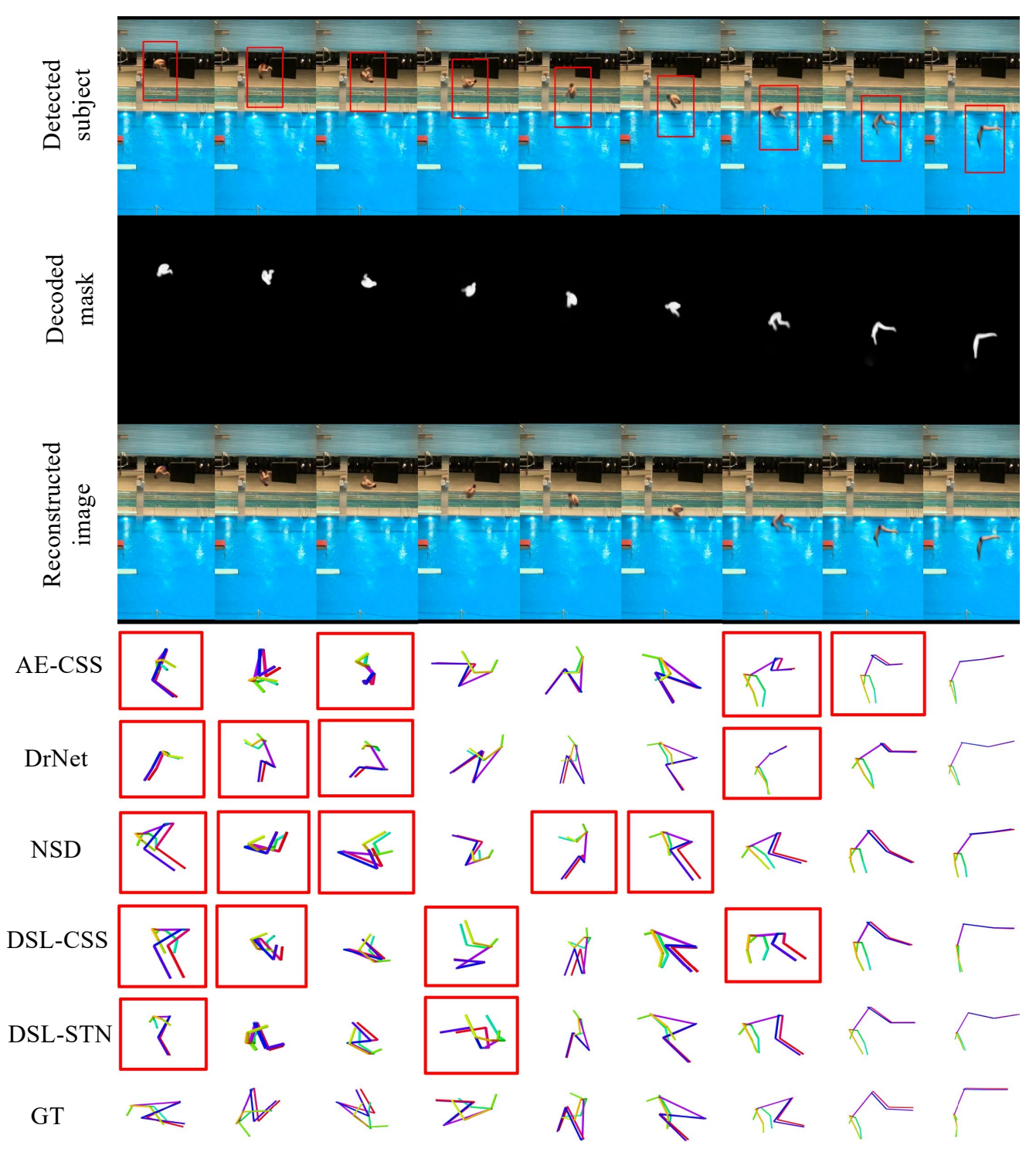


Figure S4. **Qualitative results on Diving Dataset**. Samples are taken from the test set. In the top row, the red rectangle shows the bounding box detected by our model for image cropping. The second and third rows, show respectively the decoded mask and image. Bottom rows, show the pose estimation by different models, where the red rectangle indicates pose estimation with a high error. GT in the bottom row indicates the ground truth labels.

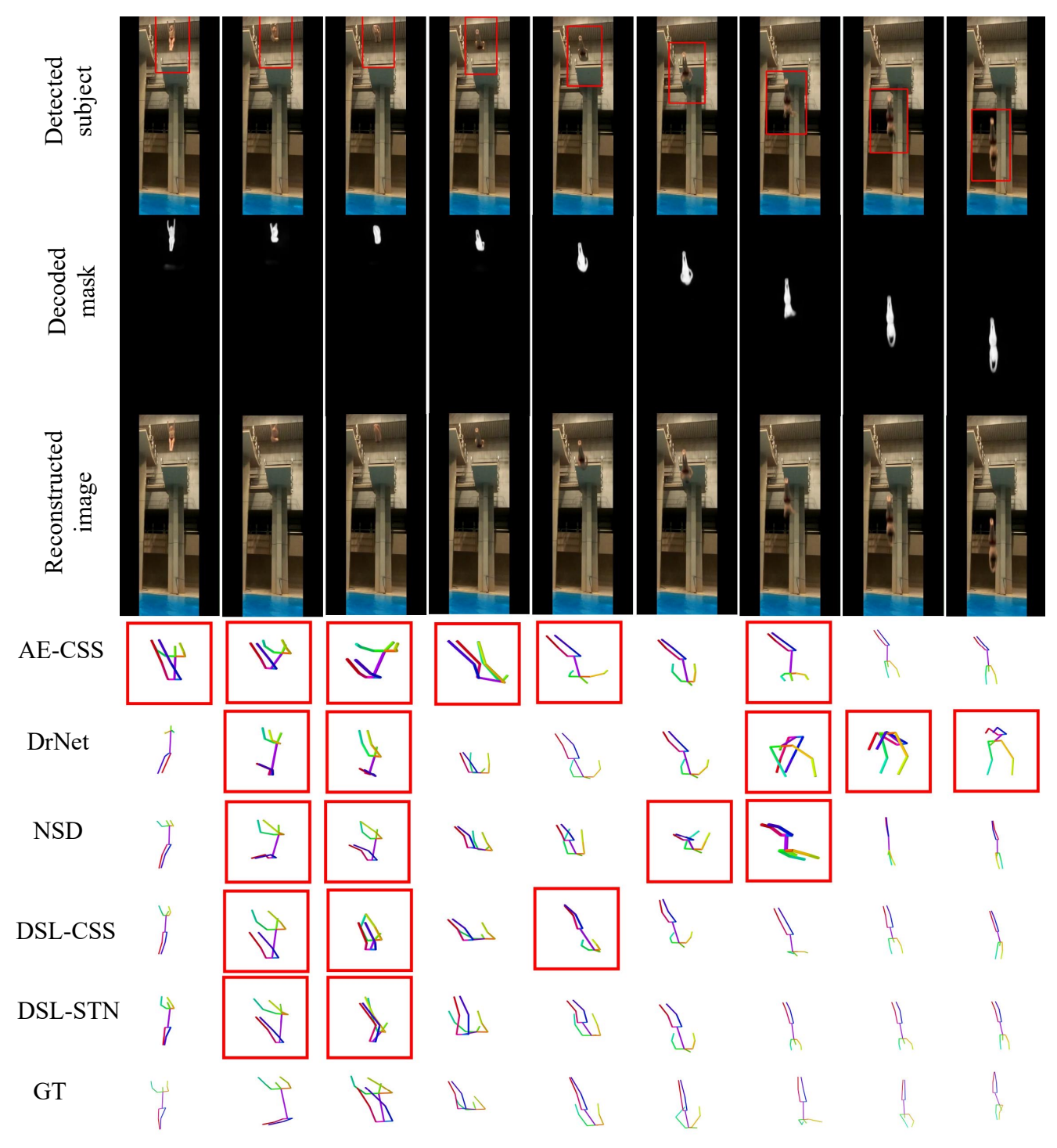


Figure S5. Qualitative results on Diving Dataset. Samples are taken from the test set. In the top row, the red rectangle shows the bounding box detected by our model for image cropping. The second and third rows, show respectively the decoded mask and image. Bottom rows, show the pose estimation by different models, where the red rectangle indicates pose estimation with a high error. GT in the bottom row indicates the ground truth labels.

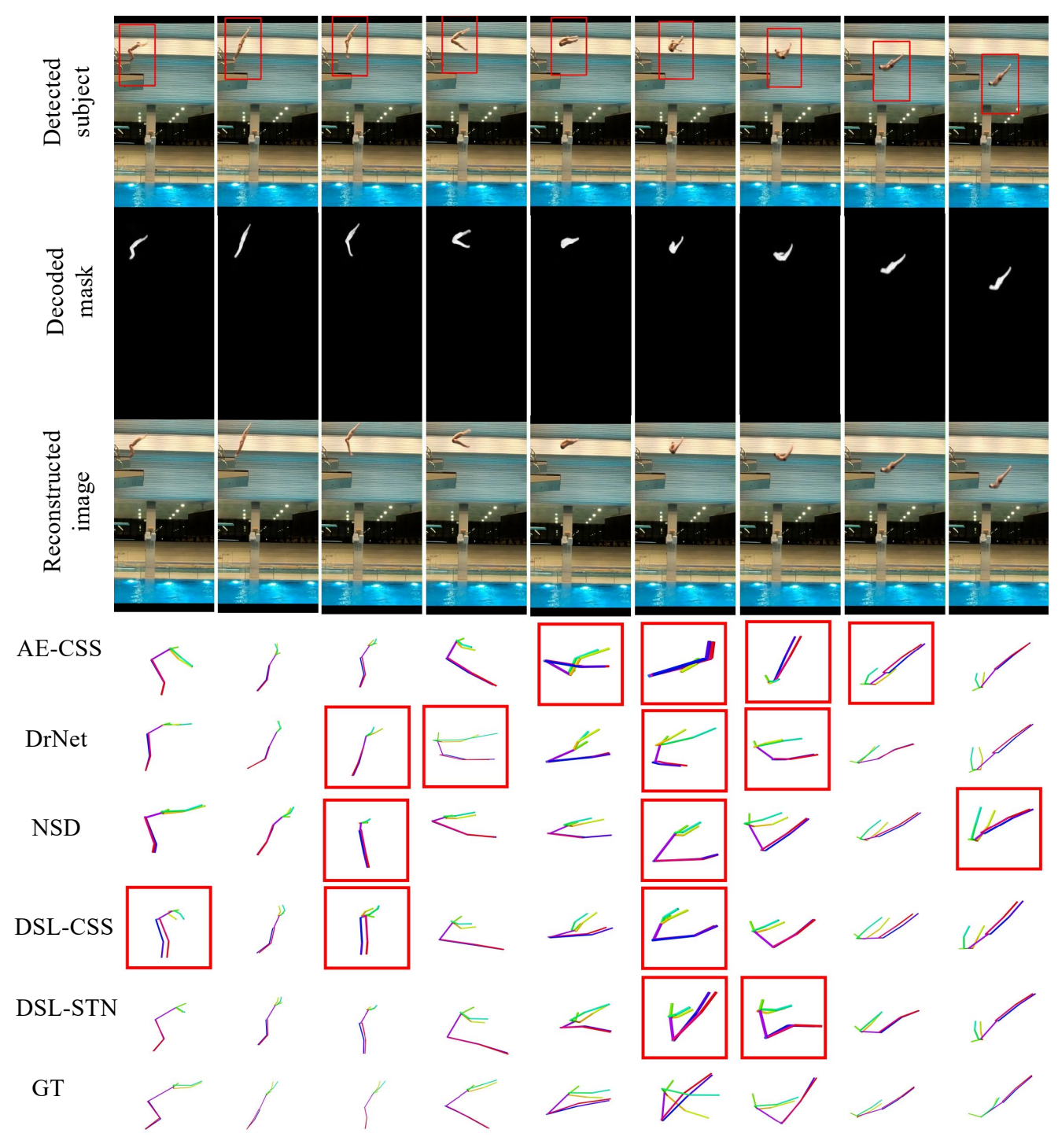


Figure S6. **Qualitative results on Diving Dataset**. Samples are taken from the test set. In the top row, the red rectangle shows the bounding box detected by our model for image cropping. The second and third rows, show respectively the decoded mask and image. Bottom rows, show the pose estimation by different models, where the red rectangle indicates pose estimation with a high error. GT in the bottom row indicates the ground truth labels.

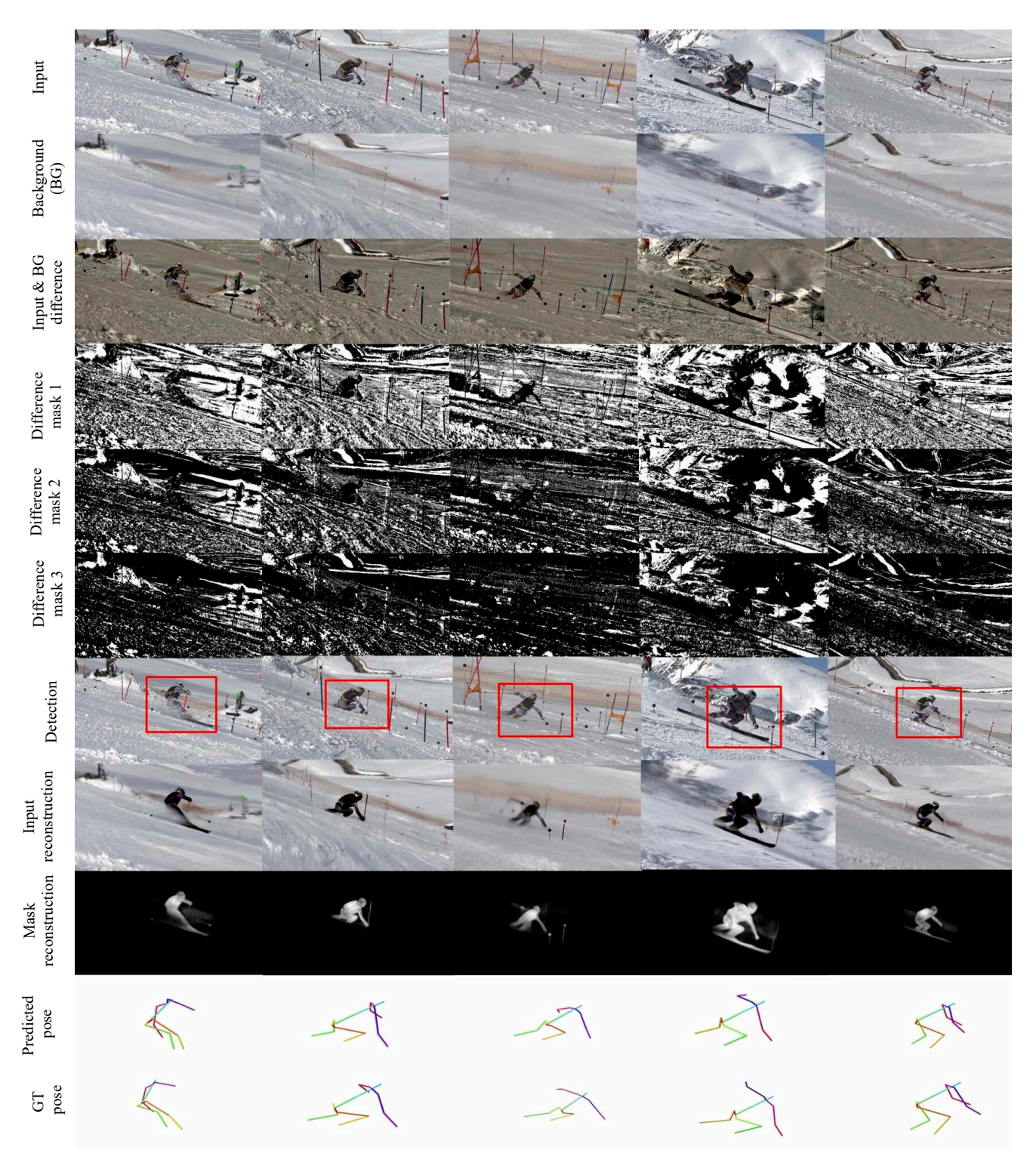


Figure S7. **Ski dataset test samples.** In the top two rows we show the input image and our estimated background on some sample images. In the third row we show the background subtracted input image. As can be observed the background is still present in the image. We also apply thresholding to this image and create masks by using three different thresholds. The resulted images are shown in rows 4 to 6. The thresholding still does not remove the background and even increasing the threshold does not help. In the next four rows we show the output of our model, which are detected subject bounding box, the reconstructed image, the predicted mask, and finally the estimated pose.

 $\mathbf{v}_0t + \mathbf{p}_0$ , where  $\mathbf{g}$ ,  $\mathbf{v}_0$ , and  $\mathbf{p}_0$  respectively indicating initial speed, initial location and gravity. We can write the projection of the center of gravity CG in the image plane in projective coordinates as

$$\mathbf{p}_{\text{proj}} = [p_{\text{proj}}^x, p_{\text{proj}}^y, p_{\text{proj}}^z] = \mathbf{K}[\mathbf{R}|\mathbf{T}](0.5\mathbf{g}t^2 + \mathbf{v}_0t + \mathbf{p}_0),$$
(15)

where  $\mathbf{g}$ ,  $\mathbf{v}_0$ , and  $\mathbf{p}_0$  are represented in homogeneous coordinates, each being a column vector of  $4 \times 1$ . this yields

$$\begin{bmatrix} p_{\text{proj}}^x \\ p_{\text{proj}}^y \\ p_{\text{proj}}^z \end{bmatrix} = \begin{bmatrix} \mathbf{K}_1^T [\mathbf{R} | \mathbf{T}] (0.5 \mathbf{g} t^2 + \mathbf{v}_0 t + \mathbf{p}_0) \\ \mathbf{K}_2^T [\mathbf{R} | \mathbf{T}] (0.5 \mathbf{g} t^2 + \mathbf{v}_0 t + \mathbf{p}_0) \\ \mathbf{K}_3^T [\mathbf{R} | \mathbf{T}] (0.5 \mathbf{g} t^2 + \mathbf{v}_0 t + \mathbf{p}_0) \end{bmatrix}$$
(16)

where  $\mathbf{K}_{i}^{T}$  is the *i*-th row of matrix  $\mathbf{K}$ . The observed x and y locations are then equal to

$$p^x = p_{\rm proj}^x/p_{\rm proj}^z, \quad p^y = p_{\rm proj}^y/p_{\rm proj}^z \ . \label{eq:proj}$$

When the image plane is parallel to the plane in which the subject travels or in orthographic projection, the depth  $p_{\rm proj}^z$  remains fixed or is ignored in the course of dive, so we can treat is as a constant c. In this case, we then get

$$\begin{bmatrix}
p^{x} \\
p^{y}
\end{bmatrix} = \frac{1}{c} \begin{bmatrix}
\mathbf{K}_{1}^{T}[\mathbf{R}|\mathbf{T}](0.5\mathbf{g}t^{2} + \mathbf{v}_{0}t + \mathbf{p}_{0}) \\
\mathbf{K}_{2}^{T}[\mathbf{R}|\mathbf{T}](0.5\mathbf{g}t^{2} + \mathbf{v}_{0}t + \mathbf{p}_{0})
\end{bmatrix}$$
(17)

Getting the second order derivative yields

$$\begin{bmatrix} a^x \\ a^y \end{bmatrix} = \frac{1}{c} \begin{bmatrix} \mathbf{K}_1^T [\mathbf{R} | \mathbf{T}] \mathbf{g} \\ \mathbf{K}_2^T [\mathbf{R} | \mathbf{T}] \mathbf{g} \end{bmatrix}$$
(18)

with  $a^x$  and  $a^y$  being acceleration in x and y directions. This makes acceleration a constant value dependent on intrinsic K, rotation R, translation T, and gravity g, hence not a function of time t. In this case, our assumption of constant acceleration strictly holds.

On the other hand, if the subject travels on a plane not parallel to the image plane, the depth of observed location changes over time, making it a function of t. In this case for y location we have  $(p^x)$  is obtained similarly)

$$p^{y} = \frac{p_{\text{proj}}^{y}}{p_{\text{proj}}^{z}} = \frac{\mathbf{K}_{2}^{T}[\mathbf{R}|\mathbf{T}](0.5\mathbf{g}t^{2} + \mathbf{v}_{0}t + \mathbf{p}_{0})}{\mathbf{K}_{3}^{T}[\mathbf{R}|\mathbf{T}](0.5\mathbf{g}t^{2} + \mathbf{v}_{0}t + \mathbf{p}_{0})}$$
(19)

Getting derivative w.r.t t we have

$$v^{y} = \frac{\partial p^{y}}{\partial t} = (20)$$

$$\frac{\mathbf{K}_{2}^{T}[\mathbf{R}|\mathbf{T}](\mathbf{g}t + \mathbf{v}_{0})(p_{\text{proj}}^{z}) - \mathbf{K}_{3}^{T}[\mathbf{R}|\mathbf{T}](\mathbf{g}t + \mathbf{v}_{0})(p_{\text{proj}}^{y})}{(p_{\text{proj}}^{z})^{2}} = \frac{(p_{\text{proj}}^{z}\mathbf{K}_{2}^{T} - p_{\text{proj}}^{y}\mathbf{K}_{3}^{T})([\mathbf{R}|\mathbf{T}](\mathbf{g}t + \mathbf{v}_{0}))}{(p_{\text{proj}}^{z})^{2}}$$

Getting second derivative w.r.t t we obtain

$$a^{y} = \frac{\partial v^{y}}{\partial t} = \frac{(21)^{y}}{(p_{\text{proj}}^{z}\mathbf{K}_{2}^{T} - p_{\text{proj}}^{y}\mathbf{K}_{3}^{T})([\mathbf{R}|\mathbf{T}]\mathbf{g})(p_{\text{proj}}^{z})^{2}}{(p_{\text{proj}}^{z})^{4}} - \frac{(p_{\text{proj}}^{z}\mathbf{K}_{2}^{T} - p_{\text{proj}}^{y}\mathbf{K}_{3}^{T})([\mathbf{R}|\mathbf{T}](\mathbf{g}t + \mathbf{v}_{0}))}{(p_{\text{proj}}^{z})^{4}} = \frac{p_{\text{proj}}^{z}(p_{\text{proj}}^{z}\mathbf{K}_{2}^{T} - p_{\text{proj}}^{y}\mathbf{K}_{3}^{T})[\mathbf{R}|\mathbf{T}](p_{\text{proj}}^{z}\mathbf{g} - (2(\frac{\partial}{\partial t}p_{\text{proj}}^{z})(\mathbf{g}t + \mathbf{v}_{0})))}{(p_{\text{proj}}^{z})^{4}}$$

As can be seen in the last line of Eq.(21), both the nominator and denominator depend on  $p_{\text{proj}}^z$ , which is the depth. It changes over time and is therefore a function of t. This violates our assumption that the acceleration is constant in the image plane when the subject moves in a plane not parallel to the image plane. However,  $p_{\text{proj}}^z$  only changes slowly for points far away from the camera because perspective projection gets increasingly close to orthographic projection as one moves away from the camera.

## S.4. Model Architecture and Training

We use an input image resolution of size  $500 \times 500$  in H36 and MPI datasets,  $500 \times 1000$  in Diving dataset, and  $640 \times 360$  in Ski dataset. To implement the STN S of Section. 3.1, we use a ResNet18 [8] that takes as input, the input image downsampled by a factor 4 in both dimensions and returns  $S(\mathbf{I}) = (s^x, s^y, u^x, u^y)$ . This is used to crop a patch  $I_{crop}$  that is then resized to  $128 \times 128$  using the affine-grid function of pyTorch. We use a ResNet50 [8] model as the encoder for both  $\mathcal{E}_{ti}$  and  $\mathcal{E}_{tv}$ , which share parameters, except in the output layer, where  $I_{ti}$  has a resolution of 129 and  $I_{tv}$  has a resolution of 600, following the settings applied in [22]. In the decoder  $\mathcal{D}$ ,  $\mathbf{I}_{tv}$  features are first passed to a fully-connected layer with ReLU and dropout with an output size of 32,768, which is then reshaped to 128 feature maps of resolution  $16 \times 16$ . The  $\mathbf{I}_{ti}$  features are passed to another fully-connected layer with ReLU and dropout to produce an output of shape  $128 \times 16^2$ . The two feature maps are then concatenated into a feature map of size  $256 \times 16^2$ . This feature map is then passed to three upsampling layers, each with one bilinear upsampling with factor 2 and three convolutional layers with kernel size  $3 \times 3$ . This upsamples the features maps from  $256 \times 16^2$ , in order, to  $128 \times 32^2$ ,  $64 \times 64^2$ , and finally to  $32 \times 128^2$ . A final convolutional layer it then applied to make the resolution of these feature maps  $4 \times 128^2$ , where the first three channels are the decoded image crop  $\mathbf{D}_{crop}$  and the last channel is the foreground subject mask crop  $M_{crop}$ . Finally, the inverse STN function is used to map the resolution of  $\mathbf{D}_{\text{crop}}$  and  $\mathbf{M}_{\text{crop}}$  to that of the original image and reconstructing the final image I according to Eq.(1).

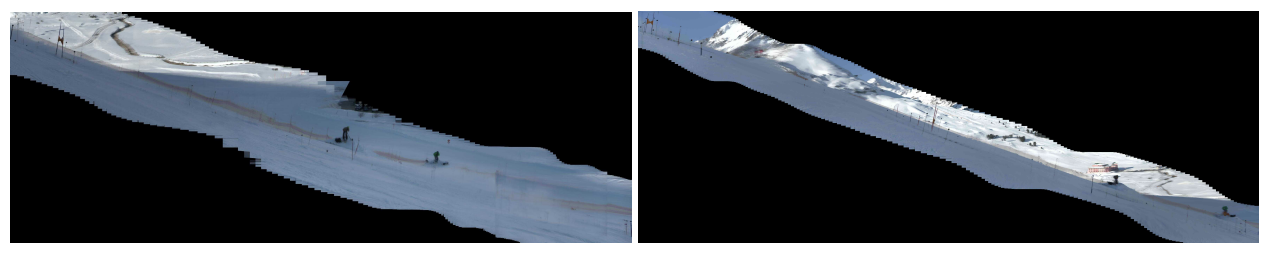


Figure S8. Ski dataset background samples. Two samples of estimated ski backgrounds are shown.

In practice, we can train this model by simply minimizing the total loss of  $\mathcal{L}_{total}$  of Eq.(7). However, convergence is very slow because it takes a long time for the STN to find the right locations for the bounding boxes. To speed up convergence, we therefore introduce priors for the bounding box locations.

H36M, MPI, and Ski. We apply a Gaussian prior on the location and size of the bounding box. We set the average detected size of the bounding box, over the mini-batch, to be about 50% of the input image resolution. On H36M we also set a prior that the location of the detected bounding box should, on average over mini-batch, be in the middle of the frame. The latter was not needed on MPI and Ski datasets. Note that these priors are applied to the average prediction of the mini-batch and not individual ones, which would otherwise imply a strong bias. We used this prior for all models except when spatial transformer network was not used in ablation study.

**Diving.** On this free-fall motion, we use the gravity loss introduced in Section 3.2 in addition to the other objectives. It requires sampling frames that are temporally equidistant. Since this sampling is different from the one required for the CSS terms and the mini-batch size is limited, we propose a two-stage training strategy. First, the network is pre-trained with  $\mathcal{L}_{DSL}^{all}$  with CSS disabled, which helps the network on the difficult task of localizing the small diver in the full-frame image. Second, we switch to CSS loss  $\mathcal{L}_{DSL}^{all}$  and its sampling for learning a precise human model for which the gravity loss is no longer required. We used the gravity prior for all models presented in Table 5, except DSL-STN (no  $\mathcal{L}_{track}$ ), in order to help them detect the diver and compare them only on the merits of other components.  $\mathcal{L}_{track}$  is only used on this dataset and we set  $\gamma$  to 1.

**Background Estimation.** As our model requires a background image, we apply the following procedure to estimate the background in each dataset. On H36M and MPI we use per-pixel median, where the median is taken over the entire video frames. On Diving dataset, we use bottom half of the first video-frame and top-half of the last frame, as the diver goes from top of the frame to the bottom in the video. On Ski dataset, homography is used to compute the background by finding SIFT correspondences between two images. By

using overlapping pairs of images, we construct a 4D image containing all of the aligned frames and we create the final background image by computing its median. Two samples of estimated backgrounds for complete ski runs are shown in Figure S8. Then for each input frame, we crop the corresponding location from the estimated background images.

**Hyper-parameters.** On H36M, MPI, and Diving datasets we set  $\lambda$  and  $\rho$  coefficients to 2. On Ski dataset to help the model better capture the foreground we reduce the rgb coefficient  $\lambda$  to 0.05 while keeping  $\rho$  at 2. This helped the model better focus on higher level image features and hence more easily encode the skier.

We set  $\alpha$  to 0.05 on H36M, and to 0.01 on MPI, diving, and ski datasets. We used the following temporal distance for sampling in models that use contrastive loss: In H36M, we used a maximum of 10 temporal frame distance for positive samples and a minimum of 200 for negative samples. In MPI, we used 10 for positive and 450 for negative samples. In Diving and Ski datasets poses change more quickly within few frames, so in Ski we use 5 for positive and 40 for negative samples whereas in Diving we use 3 for positive and 20 for negative samples. These hyper-parameters were selected based on how fast the poses change in the videos and the quality of image-reconstruction in the self-supervised models, which is our early-stopping criteria in the self-supervised model. We used the same sampling procedure for all models that use a contrastive loss.

**Pose Model.** For 3D pose estimation model in all datasets we followed the same setting used in [22] and applied two hidden layers of size 2048 with 50% dropout applied to each hidden layer. The output layer dimension is  $3 \times K$ , where K is the number of joints which is equal to 17 in H36M and Ski datasets, and to 13 in Dive and MPI datasets.

## S.5. Limitations

Our current formulation is limited to one subject of interest. Extension to multiple subjects is left for future work.

While on the Ski dataset we show the camera does not need to be static, however, a background image is still required to be computed even through the estimation is noisy. The usage of background enables our model to focus on the foreground subject when encoding latent features.